Science of the Total Environment 839 (2022) 156335

Contents lists available at ScienceDirect

Science of the Total Environment

journal homepage: www.elsevier.com/locate/scitotenv

Study of an Arctic blowing snow-induced bromine explosion event in Ny-Ålesund, Svalbard

Douxing Chen [a,b], Yuhan Luo [a,*], Xin Yang [c], Fuqi Si [a], Ke Dou [a], Haijin Zhou [a], Yuanyuan Qian [a,b], Chunqiao Hu [a,b], Jianguo Liu [a], Wenqing Liu [a]

[a] Key Laboratory of Environmental Optics and Technology, Anhui Institute of Optics and Fine Mechanics, Hefei Institutes of Physical Science, Chinese Academy of Sciences, Hefei 230031, China
[b] University of Science and Technology of China, Hefei 230026, China
[c] British Antarctic Survey, Natural Environment Research Council, Cambridge CB3 0ET, UK

HIGHLIGHTS

- Bromine monoxide plays an important role in ozone depletion in polar regions.
- MAX-DOAS observed a bromine surge at the Arctic Yellow River Station in spring 2017.
- Satellite databases and models provide insights into the bromine explosion cause.
- Blowing-snow-sourced sea salt aerosols affected by cyclones cause bromine explosion.
- High-resolution ground-based measurements improve model outcomes.

GRAPHICAL ABSTRACT

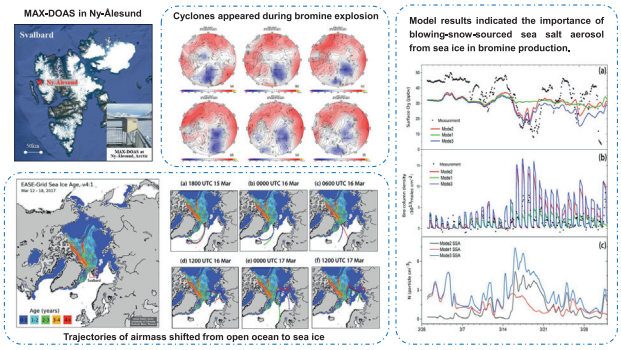

ARTICLE INFO

Editor: Jianmin Chen

Keywords:
Bromine explosion event
Ozone
Arctic
DOAS
Cyclone
Sea salt aerosol

ABSTRACT

Bromine explosion events (BEEs) are important processes that influence the atmospheric oxidation capacity, especially in the polar troposphere during spring. Although sea ice surface is thought to be a significant bromine source, bromine release mechanisms remain unclear. High-resolution ground-based observations of reactive bromine, such as BrO, are important for assessing the potential impacts on tropospheric ozone and evaluating chemical models. However, previous model studies paid little attention to Svalbard, which is surrounded by both open ocean and sea ice. In this paper, we present continuous BrO slant column densities and vertical column densities derived by Multi-Axis Differential Optical Absorption Spectroscopy deployed at Ny-Ålesund (78.92°N, 11.93°E) in March 2017. We focused on one BEE in mid-March, during which the vertical column densities of BrO surged from 4.26×10^{13} molecular cm^{-2} to the peak at 1.23×10^{14} molecular cm^{-2} on March 17, surface ozone depleted from a background level of 46.25 parts per billion by volume (ppbv) to 13.9 ppbv. This case study indicates that the BEE was strongly associated with blowing snow induced by the cyclone systems that approached Svalbard from March 14 to 18. By considering meteorological conditions, sea ice coverage, and airmass trajectory history, we demonstrate that sea salt aerosols (SSAs) from blowing snow on sea ice, rather than from open ocean, are attributed to the occurrence of this BEE. Model results from a parallelized-tropospheric offline model of chemistry and transport (p-TOMCAT) indicate that this BEE was mainly triggered by a blowing snow event associated with a low-pressure cyclone system. The concentration of blowing-snow-sourced SSAs surged to peak when the airmass pass across the sea-ice-covered area under high wind speed, which is a critical factor in the process of bromine explosion observed in Ny-Ålesund. Due to the coarse resolution, the possible delayed timing of bromine release from SSA and the model-data discrepancies still exist.

* Corresponding author.
E-mail address: yhluo@aiofm.ac.cn (Y. Luo).

http://dx.doi.org/10.1016/j.scitotenv.2022.156335
Received 15 February 2022; Received in revised form 21 April 2022; Accepted 25 May 2022
Available online 30 May 2022

1. Introduction

Halogen species in the troposphere are oxidizers that cause ozone depletion. Ozone depletion events (ODEs), where near-surface ozone concentration drops below 10 ppbv (part per billion by volume) reaching close to 0 ppbv, are typically tied to the release of significant levels of reactive bromine (e.g., Br_2, BrO, and HOBr) in the polar spring, that is, March to May in the Arctic (Barrie et al., 1988; Bottenheim and Chan, 2006; Oltmans et al., 1989). During spring, sunlight is an essential condition for photochemical reactions. Bromine radicals (BrO_X = BrO + Br) can affect boundary layer NOx (=NO + NO_2) (Morin et al., 2008) and HO_X (=OH + HO_2) (Brough et al., 2019), thereby influencing the atmospheric oxidation capacity (e.g., Abbatt et al., 2012; Willis et al., 2018) and can also affect the Arctic ecosystem by oxidizing elemental mercury (Hg^0) to reactive gaseous elemental mercury (RGM) (Holmes et al., 2010; Van Dam et al., 2013).

Bromine radicals can be conserved via self-reaction (BrO + BrO), cross-reaction (BrO + IO/ClO), and the catalytic cycle (BrO + HO_2), which destroy ozone at times. However, none of these processes can alter the abundance of the bromine family (Simpson et al., 2015), which is believed to be derived from photochemical and heterogeneous reactions of bromides (Adams et al., 2002). The specific sequence called "bromine explosion" event (BEE) is expressed mainly through the following reactions (Simpson et al., 2007b):

$$HOBr + Br^-(aq) + H^+(aq) + hv \rightarrow Br_2 + H_2O \quad (R1)$$

$$Br_2 + hv \rightarrow 2Br \quad (R2)$$

$$Br + O_3 \rightarrow BrO + O_2 \quad (R3)$$

$$BrO + HO_2 \rightarrow HOBr + O_2 \quad (R4)$$

The required saline substrates and surfaces for (R1) could be frost flowers that grow on newly formed sea ice in open leads or polynyas (Kaleschke et al., 2004), first-year sea ice (Simpson et al., 2007a; Wagner et al., 2007), perennial sea ice (Huang et al., 2020), snowpack with sea salt deposition (Pratt et al., 2013; Toyota et al., 2014), and sea salt aerosols (SSAs) generated from blowing snow (Yang et al., 2020; Yang et al., 2008; Yang et al., 2010).

Satellite-based UV–visible nadir instruments, such as GOME, GOME-2, OMI, and SCIAMACHY, are capable of capturing the temporal and spatial distribution characteristics of BrO on a global scale and in long-term observations (Begoin et al., 2010; Theys et al., 2011; Wagner et al., 2001). Satellite measurements are more sensitive to tropospheric BrO in polar regions than in other regions because of the relatively high surface albedo of snow and ice (Choi et al., 2012). However, owing to the limited resolution and specific viewing geometry, satellite measurements often underestimate BrO appearing in shallow layers below clouds (Sihler et al., 2012). Ground-based optical remote sensing instruments, including Multi-Axis Differential Optical Absorption Spectroscopy (MAX-DOAS) and long-path DOAS have advantages in terms of temporal coverage and vertical structure resolution, allowing us to investigate the BEE mechanisms in the boundary layer (Frieß et al., 2011; Honninger and Platt, 2002; Peterson et al., 2015). However, previous studies based on high-resolution MAX-DOAS observation were mostly focused on e.g. Barrow, Alaska, Eureka and Alert, Canada (e.g. Bognar et al., 2020; Honninger and Platt, 2002; Peterson et al., 2017; Simpson et al., 2017; Zhao et al., 2016), and little research has been conducted on BEEs and ODEs at Ny-Ålesund, Svalbard, where the geographic situation is different from the above locations. For instance, due to the warm North Atlantic Current, Svalbard has a relatively higher air temperature and more abundant water vapor than other Arctic areas (Zhenbo et al., 2008). Thus, there is less sea ice coverage to the south of Svalbard in the Norwegian Sea (as described in Section 2.1 and Fig. 1). However, spring BEEs are frequently observed in this region (Luo et al., 2018). Therefore, it is worth investigating and discussing whether the open-ocean-sourced SSA plays the same role as the sea-ice-sourced SSA and whether the mechanism parameterizations implemented in models work at this specific location.

Numerical models are crucial for exploring the processes involved in BEEs and ODEs (Simpson et al., 2007b). In recent years, based on observations and field experiments conducted in polar regions, reactive halogen chemistry schemes, including BrO releasing mechanisms have been developed in various models (Choi et al., 2018; Huang et al., 2020; Marelle et al., 2021; Toyota et al., 2014; Yang et al., 2010). Observations of tropospheric BrO can provide useful information for examining the simulation of the BEE. Global and regional models with various emission schemes of halogen chemistry have been implemented to simulate BrO column enhancements over sea ice and coastal areas, and they generally compare well with large-scale BrO observations, mostly satellite-based measurements, and airplane-based field campaign data (Choi et al., 2018; Huang et al., 2020; Marelle et al., 2021; Theys et al., 2011; Yang et al., 2010).

However, the details of the emission process of BrO and the trigger criteria of meteorology, the role of snowpack or sea ice are not well constrained and remain unclear. For instance, BrO enhancements can be observed either under blizzard conditions or in a stable boundary layer (Jones et al., 2009). Ground-based observations indicated the periods of BrO column enhancement came with an increase in aerosol extinction (Frieß et al., 2004; Frieß et al., 2011). Under high-speed conditions (>7m s^{-1}), salty snow particles on sea ice can be blown up and sublimated to produce airborne SSAs as a direct source of bromine (Frey et al., 2020; Yang et al., 2020; Yang et al., 2008; Yang et al., 2010). In this case, the long-range transportation of bromine-enriched air from its source region may play an important role in BEE observations. At low wind speeds, the release of reactive bromine is connected to snowpack over tundra inland and sea ice (Peterson et al., 2018; Pratt et al., 2013; Simpson et al., 2017; Toyota et al., 2011). The recent modeling work by Marelle et al. (2021), using the Weather Research and Forecasting coupled with Chemistry (WRF-Chem) model with both snowpack and blowing snow-sourced bromine activation mechanisms, showed that these two mechanisms could cause ODEs; however, the blowing snow mechanism induces ODEs only under specific windy conditions.

High-resolution ground-based observations are important for evaluating chemical models and improving our understanding of their potential impacts on tropospheric ozone and oxidizing capacity. In this article, we investigate the observational results from the MAX-DOAS deployed at the Arctic Yellow River Station for March 2017 particularly focusing on a BEE case (from March 15 to 19) for further study.

The method section contains details on how the remote-sensing BrO data were derived and the p-TOMCAT model used in the study, and other complementary data such as meteorological conditions, sea ice coverage, and the back trajectory model, which will be used in the diagnosis and data interpretation. The results and discussions are presented in Section 3, and the conclusions are presented in Section 4.

2. Methods - data and modeling

2.1. MAX-DOAS

In this work, MAX-DOAS, located at the Arctic Yellow River Station (78.92°N, 11.93°E), was used for trace gas measurements. The specific instrument site is in Ny-Ålesund on the west coast of Svalbard, 30 m above sea level, as shown in Fig. 1a. Unlike other Arctic stations such as Barrow (Alaska), Alert (Nunavut), and Eureka (Canada), the Ny-Ålesund station (Svalbard) is not completely surrounded by sea ice, as open water exists in the south of Svalbard throughout the year (Fig. 1b) because of the influence of the North Atlantic Current. Besides, as demonstrated in Fig. 1b, the Arctic Ocean is primarily covered by first-year sea ice in the northeast of Svalbard, and the adjacent northwestern areas and southeast of Greenland are partly covered by multi-year sea ice.

MAX-DOAS, operated in Ny-Ålesund, comprises both outdoor and indoor parts. The outside telescope is controlled by a stepper motor that can modify the elevation angles from the horizon to the zenith. The field

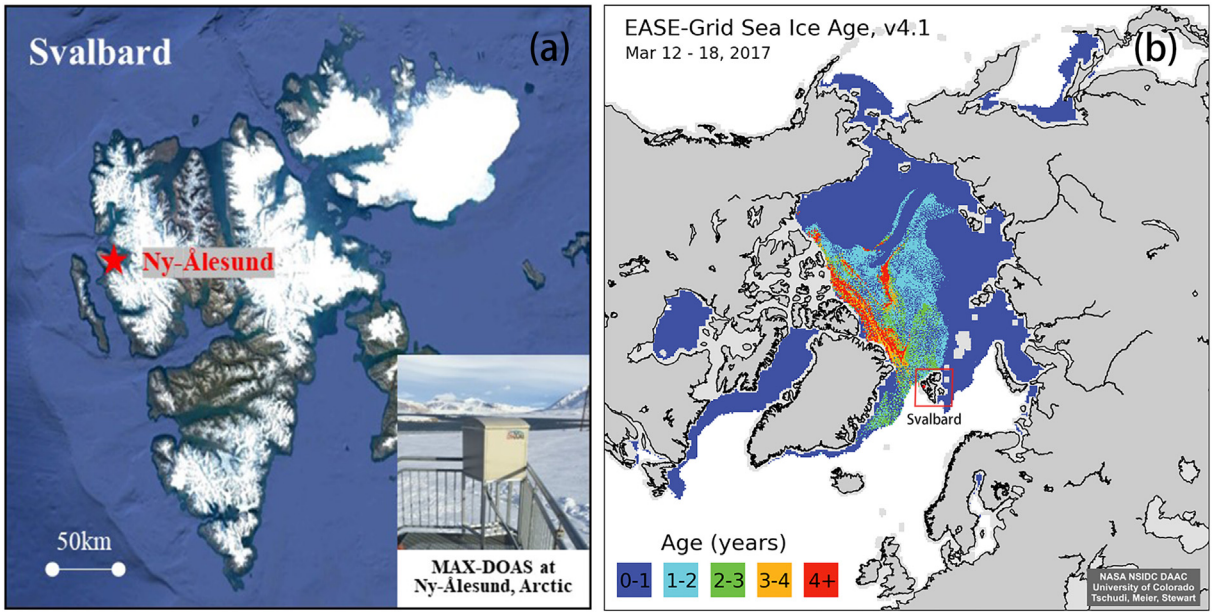

Fig. 1. (a) Location of ground-based MAX-DOAS in Ny-Ålesund, Svalbard, (b) Sea ice coverage and age in the Arctic during 12 March–18 March 2017. The area in (a) is marked in (b) by the red frame.

of view of the telescope was 1°, and the sequence of elevation angles was 2°, 3°, 4°, 6°, 8°, 10°, 15°, 30°, and 90°. The telescope can receive scattered sunlight from different angles as the elevation angle changes. The light was focused on a quartz fiber bundle (with a numerical aperture of 0.22) using a quartz lens. Then, the light is imported to the inside spectrograph (Ocean Optics MAYA pro), including a CCD with 2048 pixels. The spectra were recorded in the wavelength range of 290 to 429 nm, enabling the analysis of several trace gases (e.g., O_4, BrO, OClO, NO_2). The spectral resolution (FWHM) is approximately 0.5 nm. The integration time ranged from 100 to 2000 ms, depending on the intensity of the light. The entire spectrometer was heated to + 20 °C using a thermal controller to ensure the normal functions of the instrument.

2.2. Data processing

We used the QDOAS software developed by the Belgian Institute for Space Aeronomy (BIRA) to calibrate the wavelength and analyze spectral information based on the DOAS method (Platt and Stutz, 2008). Specifically, MAX-DOAS spectral analysis of BrO was performed in the wavelength range between 336.5 and 359 nm, containing three absorption bands. To minimize the interference of Fraunhofer spectral lines and the effect of stratospheric contribution, we selected the zenith spectrum of every cycle as the Fraunhofer reference spectra (Hönninger et al., 2004). The settings involved in the inversion algorithm are shown in Table 1. The original cross-sections were convoluted with the instrument silt function to match the resolution of the instrument. A fifth-order polynomial was operated to remove the broad-band spectral structure caused by Rayleigh and Mie scattering. The retrieval settings of the oxygen dimer (O_4) are similar to the sets for BrO, but in the wavelength interval of 340–370 nm; detailed selections of cross-sections are shown in Table 1.

Table 1
MAX-DOAS spectral analysis setting.

Cross sections	BrO	O_4
O_3_223K (Bogumil et al., 2003)	√	√
O_3_243K (Bogumil et al., 2003)	√	√
NO_2_298K (Vandaele et al., 1998)	√	√
NO_2_220K (Vandaele et al., 1998)	√	√
O_4_273K (Thalman and Volkamer, 2013)	√	√
BrO_298K (Fleischmann et al., 2004)	√	N/A
OClO_233K (Kromminga et al., 2003)	√	N/A
Ring spectrum	√	√
Polynomial	Fifth order	

The output of the retrieval procedure is the differential slant column density (DSCD), which is the integration of trace gas concentrations along the effective light path relative to the Fraunhofer reference. The residual root mean square (RMS) of the BrO DSCD was less than 5×10^{-4}, resulting in the statistic BrO DSCD errors are typically $<2 \times 10^{13}$ molecular cm^{-2}. We used two-step calculation to convert DSCDs to vertical column density (VCD) which is defined as the integrated concentration of trace gases in the vertical direction. Firstly, air mass factor (AMF) is obtained by performing radiative transfer modeling (RTM) using SCITRAN software and the elevation angle of 30° and 90° was chosen respectively. Secondly, the difference between $AMF_{30°}$ and $AMF_{90°}$ served as DAMF for the calculation of VCD based on the following function

$$\mathrm{DAMF} = \frac{\mathrm{DSCD}}{VCD} \quad (1)$$

Regarding setting the main parameters in RTM, an exponential a priori profile (0–2 km) with a scale height of 200 m was selected for modeling calculation and the surface concentration was set to 1×10^9 molecular cm^{-3}, the wavelength was set to 338.5 nm at which has an absorption peak, surface albedo was set to 0.1, the solar zenith angles (SZA) and the solar azimuth angles (SAA) input were according to practical calculation.

2.3. p-TOMCAT model

The Cambridge parallelized-tropospheric offline model of chemistry and transport (p-TOMCAT) is a global three-dimensional chemistry transport model with a horizontal resolution of 2.825° × 2.825° (longitude × latitude) and 31 vertical layers from the surface to approximately 10 hPa (~31 km) at the top model layer. The average height of the bottom layer was approximately 60 m. The driving files (winds, temperature) for p-TOMCAT were a 6-hourly ERA-5 dataset from the European Center for Medium-Range Weather Forecasts (ECMWF). Monthly sea ice coverage and sea surface temperatures were obtained from the Hadley Center Sea Ice and Sea Surface Temperature (HadISST) dataset (Rayner et al., 2003).

The tropospheric halogen chemical scheme used in the model has been detailed in the recent work of Yang et al. (2020) and Yang et al. (2019). The

p-TOMCAT model includes two types of inorganic bromine sources: the oxidation of short-lived bromocarbons ($CHBr_3$, CH_2Br_2) (Warwick et al., 2006; Yang et al., 2014) and SSA-sourced bromine, from both open-ocean-sourced sea spray and sea-ice-sourced SSA (Yang et al., 2020; Yang et al., 2010). Snowpack bromine emissions are not considered in this model. The process-based SSA scheme for both open-ocean sourced sea spray and sea-ice-sourced SSA was implemented in the model by Levine et al. (2014). The validation of our model ability in SSA simulation has been made against airborne SSA and deposited sodium in snow (Levine et al., 2014; Rhodes et al., 2018; Rhodes et al., 2017; Yang et al., 2019). A similar work has been done in GEOS-Model by Huang and Jaeglé (2017). The SSAs are tagged in 21 size bins covering a dry diameter of 0.02–20 μm in order to track their history. Other parameters used in this study were set as: a 3.5 times salinity of Antarctic snow for the Arctic, the shape parameter of blowing snow particles $\alpha = 3$, and the scale parameter $\beta = 37.5$ μm with a SSA production ratio $N = 1$ (i.e., 1 sub-SSA particle formed from one saline-blowing snow particle during sublimation).

Given the contribution of bromocarbons to polar tropospheric bromine is very small (i.e. <1 pptv, Yang et al., 2020), we ignored their contribution and only focused on the SSA-sourced bromine in this study. In terms of bromine release from SSA, we used bromine depletion factors (DFs) to parameterize bromine release (Legrand et al., 2016; Yang et al., 2020) and simply assume they work in the same way. However, freshly emitted sea spray from the open ocean is always alkaline with a pH of ~8, whereas sea-ice-sourced SSA is mostly acidic (Frieß et al., 2004; Pratt et al., 2013; Vogt et al., 1996) due to contamination by atmospheric sulfate or nitrate therefore they could be different in terms of reactive bromine release, for example, in either timing or magnitude. Due to the lack of field data in Arctic, we cannot constrain them and evaluate this parametrization. The continuous BrO data obtained at Svalbard, where the influencing airmasses come from either the open ocean or sea ice, may enable us to perform an evaluation activity to examine this issue via a good case study.

A detailed model-data comparison was made. The model outputs of temperature, wind speed, SSA particle number concentration, concentrations of O_3 at the bottom layer, and BrO column density were compared with the observations.

2.4. Complementary datasets

2.4.1. Meteorology data

Several datasets were employed to interpret data. Continuous meteorological observations (temperature, wind speed and direction, and air pressure) were made at the Ny-Ålesund station (taken from Maturilli (2018a)). The temperature was measured using a thermometer, wind speeds and directions were measured using an anemometer, and a barometer was utilized for air pressure measurement. The cloud base height data refer to Maturilli (2018b). Ambient pressure and 10 m-vector-wind speed in the Arctic was obtained from ECMWF 6-hourly interim meteorological data (ERA-interim data). Surface ozone was measured using UV photometry at the Zeppelin station. The hourly ozone data were downloaded from the EBAS database (http://ebas-data.nilu.no/).

2.4.2. GOME-2 tropospheric BrO

The GOME-2B tropospheric columns of BrO used in this study are described in detail by Bougoudis et al. (2020). In brief, tropospheric BrO partial columns (VCD_{tropo}) were obtained based on Theys et al. (2009) to derive the total slant column densities of BrO using the DOAS method (Burrows et al., 2011) using a 338–360 nm fitting window and for

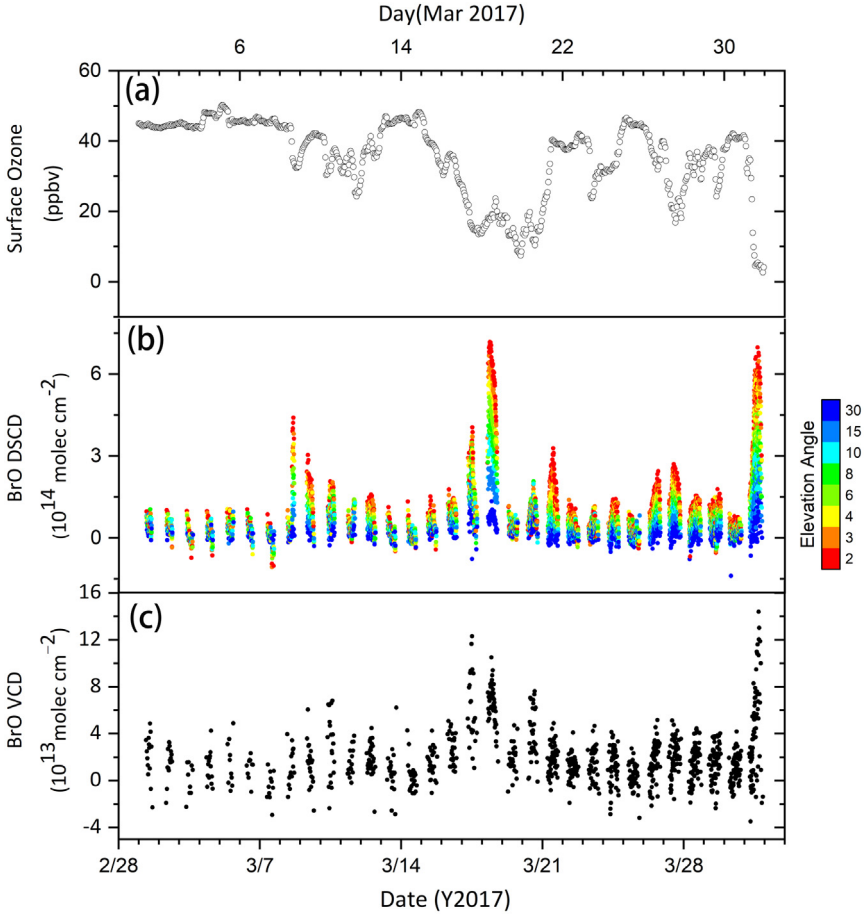

Fig. 2. (a) Surface ozone during the measurement, (b) Time series of DSCDs of BrO at different elevation angles shown in a color bar, (c) VCDs of BrO derived from BrO DSCDs at 30° elevation angle.

stratospheric separation. Stratospheric vertical densities were estimated using a stratospheric BrO climatology from the BASCOE model (Errera and Fonteyn, 2001) and National Centers for Environmental Prediction (NCEP) reanalysis data (Kalnay et al., 1996) tropopause heights. Stratospheric VCDs multiplied by a stratospheric AMF can be converted to slant densities, and easily subtracted from the total slant columns. A correction factor was used to account for the long-term reduction of bromine emissions in the stratosphere based on ground-based zenith-sky measurements of BrO over Harestua (Hendrick et al., 2008). The tropospheric AMF was also applied for conversion to VCD_{tropo}, assuming a surface albedo of 0.9 above sea ice and all tropospheric BrO is well mixed within the boundary layer (Begoin et al., 2010; Blechschmidt et al., 2016).

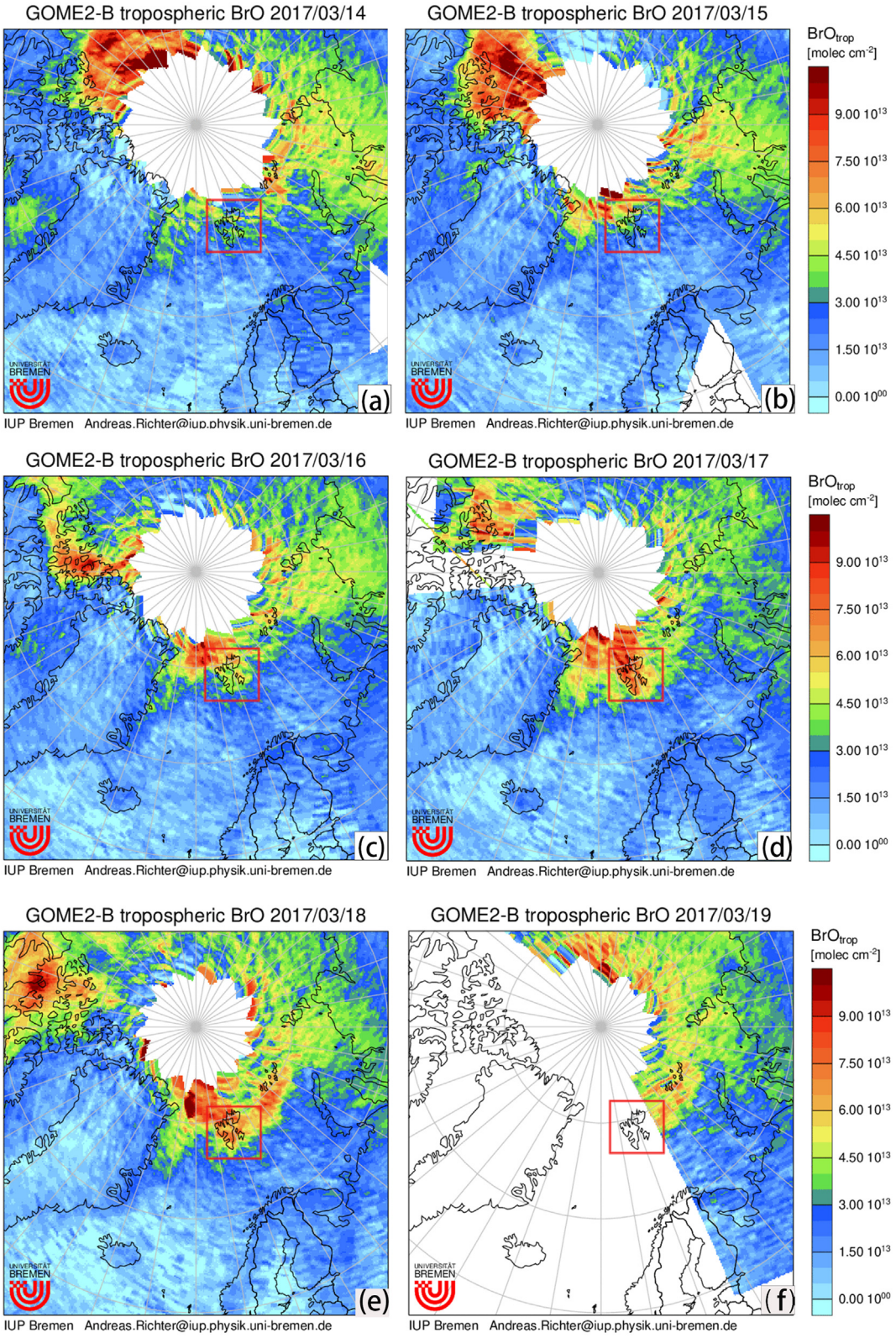

Fig. 3. GOME-2B BrO VCD_{trop} of Arctic from March 14 to 19, 2017. The red box in each panel indicates the location of Svalbard.

2.4.3. Airmass trajectory

To investigate the origin of the bromine-enriched airmass approaching Ny-Ålesund, Svalbard, we run the online HYSPLIT model (https://www.ready.noaa.gov/hypub-bin/) with the Global Data Assimilation System (GDAS1) meteorological data set on a 1° × 1° grid. The Arctic Yellow River Station was established as the endpoint to process the back trajectories of the airmass at three different altitudes (50 m, 200 m, and 1 km). Since bromine explosion events are often connected with sea ice, we merged the sea ice distribution with the obtained back-trajectory data. The sea ice remote sensing data were obtained from the Advanced Microwave Scanning Radiometer-Earth Observing System (AMSR-E) onboard the Aqua satellite from NASA National Snow and Ice Data Center Distributed Active Archive Center (NASA NSIDC DAAC) (Tschudi et al., 2019).

3. Results and discussions

3.1. Observation results

3.1.1. Ground-based measurements

Following the method mentioned in Section 2.2, we retrieved the DSCDs and VCDs of BrO for March 2017 (Fig. 2). There were three obvious enhancements of BrO DSCDs peaking on March 8, 18, and 31 respectively. Each increase in BrO came with surface ozone depletion (Fig. 2a). While the accordingly peak values of BrO VCDs appeared on March 10, 17, and 31 (Fig. 2b), which might be related to the aerosol extinction. As shown in Fig. S1, O_4 DSCDs on March 10 and 17 were not well separated. In the current work, we focus on one prominent bromine explosion event that appeared during the period from March 15 to 19 for further investigation. During this BEE, the DSCD of BrO gradually rose from a background level of 1.2 × 10^{14} molecular cm^{-2} to a peak value of approximately 7.6 × 10^{14} molecular cm^{-2} on March 18, followed by a slump on the next day and then returned to normal levels. The VCD of BrO gradually increased from 4.25 × 10^{13} molecular cm^{-2} to 1.23 × 10^{14} molecular cm^{-2} on March 17 and then dramatically decreased back to 4.71 × 10^{13} molecular cm^{-2} between March 18 and March 20. Simultaneously, there was a significant decline of ozone concentration from a pre-event 46.25 to 13.9 ppbv, which recovered to the background level after midday on March 21.

3.1.2. Comparison with GOME-2B

To assess the ground-based observation results, we compared the retrieved MAX-DOAS BrO VCDs with satellite measurements. The performed linear regression analysis was shown in fig. S2. Because values of BrO VCD_{tro} in Svalbard on March 1–10, March 19 and March 21 is null, only data available in the grid whose center location is nearest to Yellow River Station were selected for comparison. These 18-day measurements indicate a high correlation between ground-based measurements and GOME-2B observations (R = 0.73) with a slope of 0.56 and offset of 1.64 × 10^{13} molecular cm^{-2}. The differences are mainly caused by the different column altitudes, the visibility conditions and the cloud interruption. For example, there was a peak value of BrO VCD at 9.18 × 10^{13} molecular cm^{-2} on March 17 for MAX-DOAS measurement, while the data from GOME-2B observation was just 5.94 × 10^{13} molecular cm^{-2}, as demonstrated in

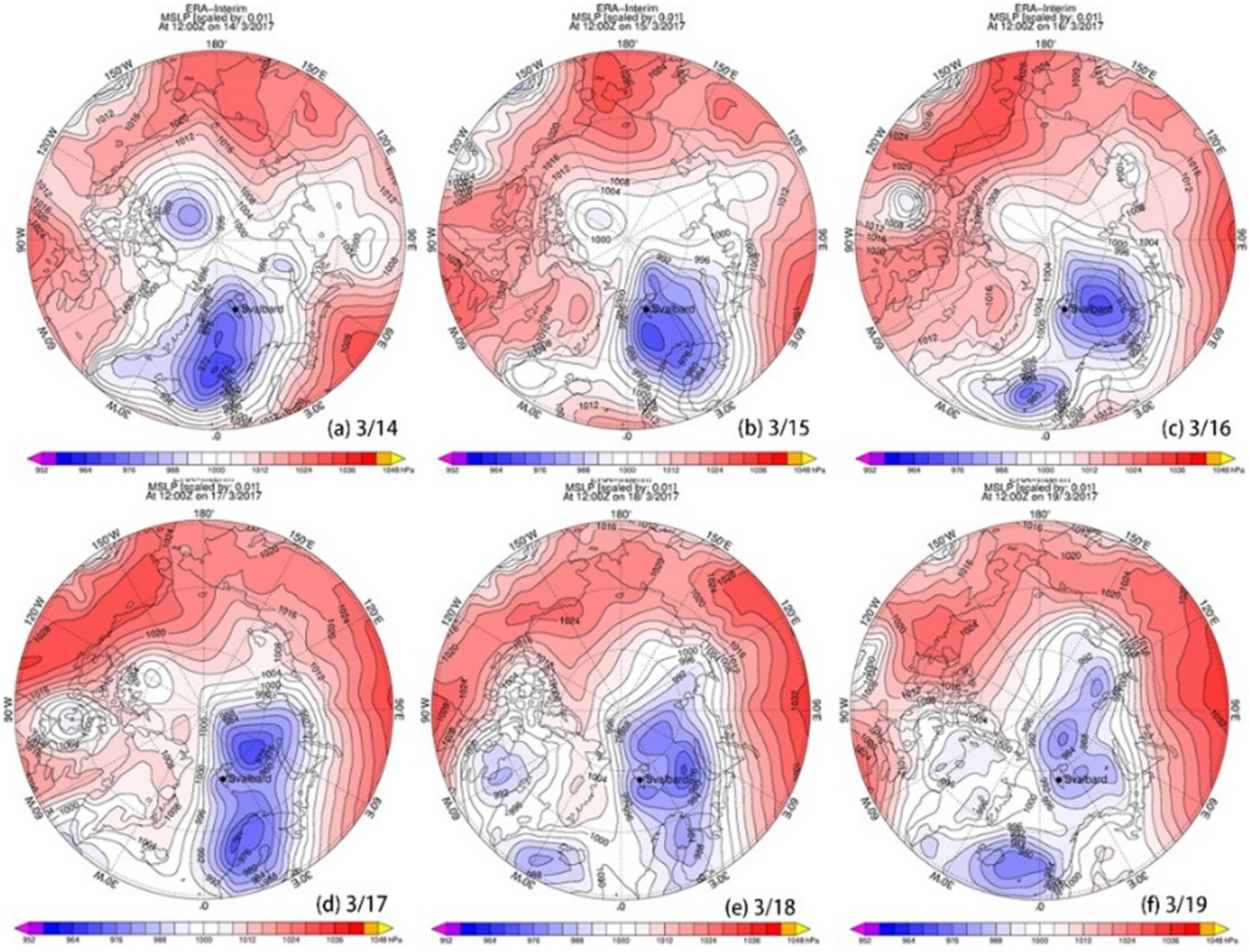

Fig. 4. Marine sea level pressure (MSLP) maps in the Arctic (from ERA-Interim data) from March 14 to 19. Svalbard is highlighted by a black dot.

Fig. S1b. This large discrepancy was highly attributed to the cloud interruption, which can also indicate bromine-enriched airmasses mostly appeared in boundary layer.

3.2. The march 15–19 bromine explosion event

According to the maps of GOME-2 tropospheric BrO (Fig. 3), the VCD_{trop} of BrO at Ny-Ålesund showed a noticeable increase from March 16 to 18, which is roughly consistent with the ground-based MAX-DOAS observations. The surge of BrO VCD_{trop} around Svalbard is starting from the north of Svalbard, above the extensive sea ice coverage, indicating the origin of BrO is from the sea ice zone. The enhancement of BrO in Svalbard lasted for about 3 days from March 16 to 18.

As shown in the variation of sea-level pressure in Arctic (Fig. 4) during the period from March 14 to 19, there was a low-pressure generated over the Norwegian Sea that moved gradually toward Svalbard. On March 15, the center of the low-pressure system was close to Svalbard, the surface pressure at the station dropped to the lowest point around 972 hPa (Fig. S3). Due to the passage of a front line, the surface wind speed at station surged to a peak value at 14.5 m s^{-1} and the wind speed over sea ice around Svalbard also showed a dramatic rise to above 10 m s^{-1} (Figs. 4b, 5b). On March 16, the cyclone moved northerly with the center of the cyclone located east of Svalbard. Simultaneously, another small low-pressure system appeared near Iceland and moved toward the north (Fig. 4c). Svalbard was then placed in the middle zone and influenced by both cyclones. During this period, wind directions at the station changed from initial southerly (before UTC 6:00 on March 16) to northerly and then back southerly after UTC 18:00 on March 17 (Fig. S3). Meanwhile, the surface wind speeds over the areas north of Svalbard in cyclone increased significantly to 14 m s^{-1} and above (Fig. 5c–d), the wind speeds at station were also at a high level of approximately 10 m s^{-1}, and air temperature continuously decreased to reach a minimum value of −22 °C at UTC 00:10 on March 18 (Fig. S3). Since March 18, the air pressure began to increase. When most of the cyclone system moved into the sea ice zone on March 19, the lower pressure system began to weaken because of losing energy supply from the bottom.

As mentioned previously, when surface wind speeds exceed a threshold value of ~7 m s^{-1}, blowing snow occurs. On sea ice, saline windblown snow particles have been found to act as a large source of reactive bromine (Blechschmidt et al., 2016; Choi et al., 2018; Frey et al., 2020; Yang et al., 2020; Yang et al., 2019; Yang et al., 2008). However, open ocean sea spray is also a large potential source of bromine (Sander et al., 2003; Yang et al., 2005). To examine their relative importance to the observed BrO enhancement, we check back trajectory HYSPLIT model results, shown in Figs. S4 and S5.

Fig. S4 shows HYSPLIT 5-day back trajectories on March 18, 2017 (ending at UTC 10:00 from three altitudes of 50 m, 200 m, and 1 km at the Arctic Yellow River Station), when BrO DSCD peak value was measured (Fig. 2b). Before the airmass approached Svalbard, they were transported within the boundary layer for a few days on sea ice (refer to Fig. 6) and then they were

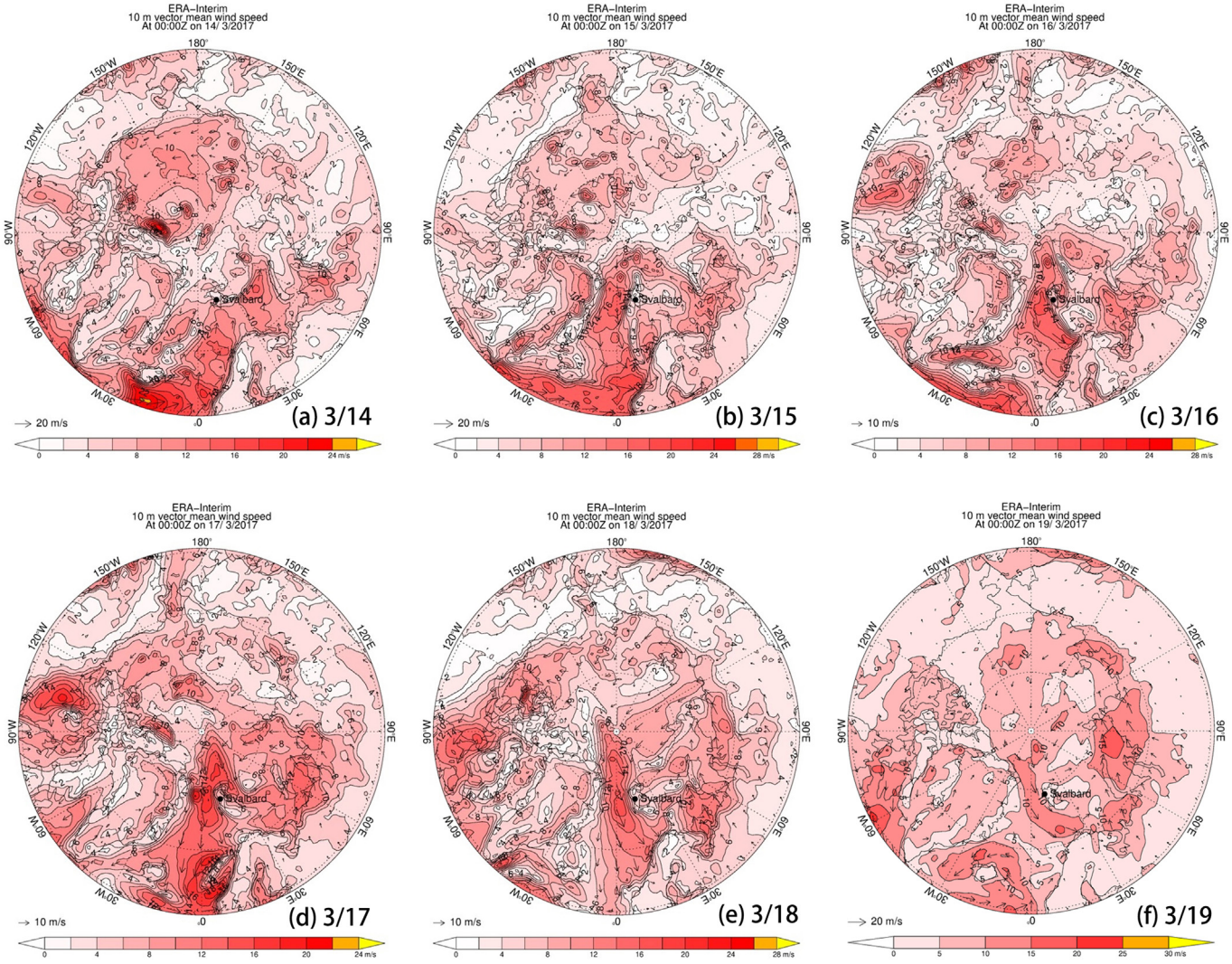

Fig. 5. Ten meter-vector-wind speed in the Arctic (from ERA-Interim data) from March 14 to 19. Svalbard is highlighted by a black dot.

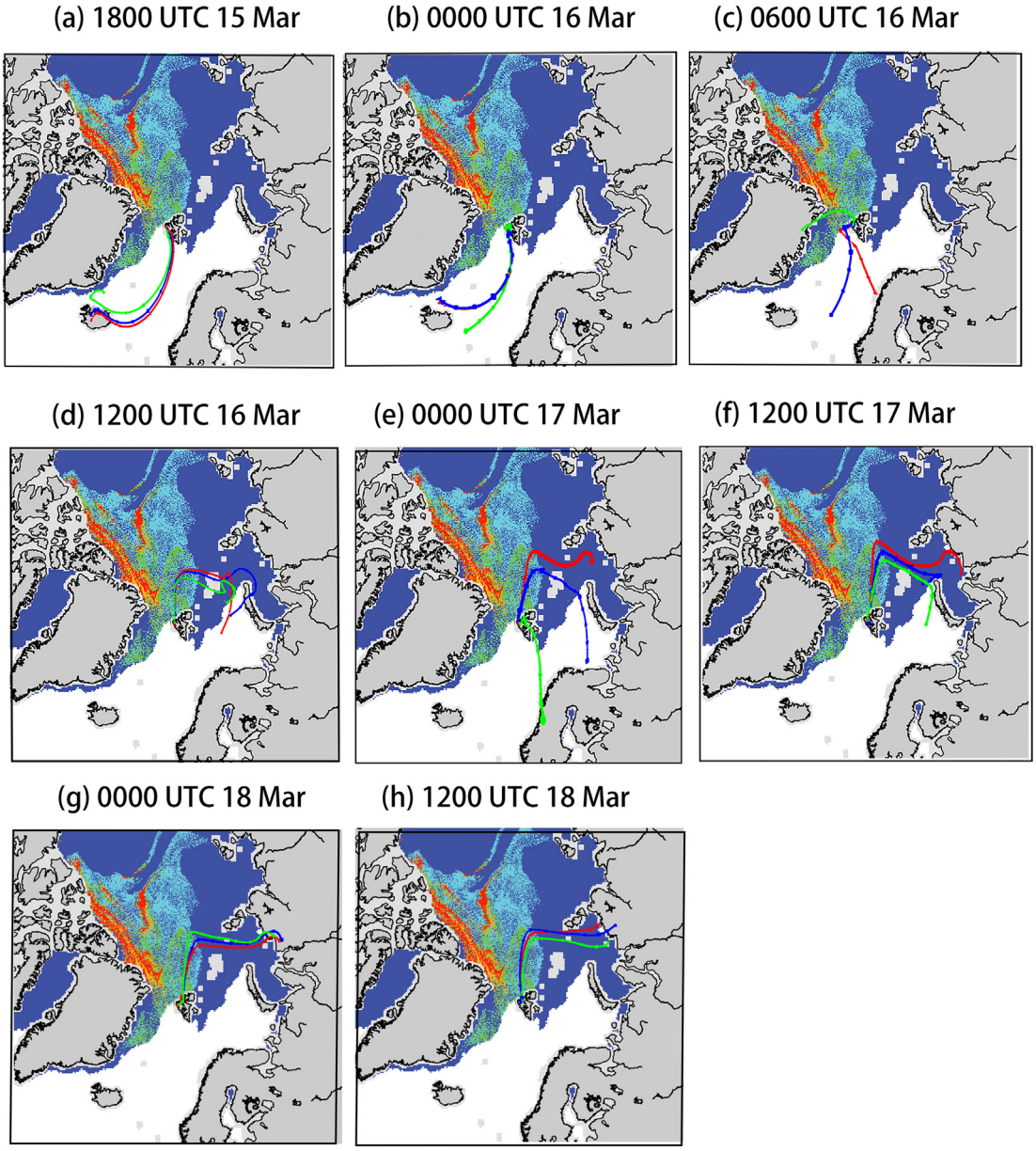

Fig. 6. Trajectories of airmass overlapped with maps of sea ice coverage. The figures above are adapted from Fig. S5 and NASA National Snow and Ice Data Center Distributed Active Archive Center (https://daacdata.apps.nsidc.org/pub/DATASETS/nsidc0611_seaice_age_v4).

uplifted to an altitude of ~1.5 km owing to the frontal lifting. Between March 15 and March 16, the transporting directions of airmasses changed, which is in accordance with the change of dominated wind direction at the station (Fig. S3, wind shifted from southeast to the north after UTC 6:00 on March 16).

Fig. 6 shows 72 h back trajectory results on top of the sea ice map between March 15 and 18. The original back trajectory maps can be found in fig. S5. Before UTC 06:00 on March 16, the airmasses traveled mainly over the open ocean in the southwest of Svalbard and were not close to sea ice (Fig. 6a–c). During this period, surface wind speeds over both open ocean and sea ice zones in the north and east of Svalbard showed a rise, the wind speeds at Yellow River Station increased from <5 m s^{-1} on early March 15 to ~15 m s^{-1} on March 16 as well (Figs. 5 and S3), the observed BrO at station still did not increase (Fig. 2), strongly indicating that open ocean sourced SSA is not an immediate source of reactive bromine. This could be due to the fact that newly emitted SSA from the open ocean is alkaline (with a pH of ~8, same as seawater), and the release of bromine from saline crystals requires acidic conditions (Abbatt et al., 2012). The acidification process for alkaline sea spray particles takes time and depends on the relative abundance of air pollutants. Thus, the actual portion of bromide that can be released from sea spray and where/when this release process may happen are complicated and not fully clear (Sander et al., 2003). This observation supplies a unique opportunity to enables us to examine these two processes acting as reactive bromine source to polar boundary layer.

As can be seen in Fig. 6d–g, from UTC 12:00 on March 16 to UTC 00:00 on March 18, the trajectories of air gradually shifted to the northeast and passed across the Barents Sea and the Kara Sea. This period coincides with the outbreak of boundary layer BrO as observed by MAX-DOAS and GOME-2, clearly indicating that the sea ice source is the direct source of reactive bromine. The type of sea ice in this area is mainly first year ice, which is beneficial to the salt supply to snowpack on sea ice (Frey et al., 2020). Although we do not have aerosol dataset, the produced SSA via sublimating saline windblown snow particles is likely the direct source of reactive bromine. From UTC 00:00 on March 18, the low-pressure cyclones became weaker and could not high enough to create blizzard conditions (Figs. 4e

and 5e), which made the direction of the airmass steady (Fig. S3). At this time, although air masses still passed over the sea ice area, the abundance of BrO did not increase further.

3.3. Source of enhanced BrO

Three p-TOMCAT simulation experiments and two sets of sensitivity experiments were performed to investigate the cause of this bromine explosion event, and the model setups are shown in Table 2.

To examine the reliability of the meteorological data used in the model, we conducted a correlation analysis between the model outputs and the corresponding meteorological parameters measured at the station (for temperature and wind speeds at 10 m height), with the results shown in Fig. S6. The correlation coefficient of temperature $R = 0.86$ (Fig. S6a, c), and the correlation coefficient of wind speed $R = 0.64$ (Fig. S6b, d). Although the model wind speed did not show perfect agreement with the measurements, with a lower bias for air temperature and higher bias for surface winds, the timings when peak values appeared were in good agreement. Owing to the coarse model resolution, the model could not represent sub-grid box-scale dynamical processes. However, the driving files used in the model are still reliable for interpreting large-scale observations.

Fig. 7 shows the simulated BrO VCD, the simulated O_3 concentration and the simulated particle number concentration of the SSA in the surface layer grid box of March 2017. When we set the open ocean as the only source of SSA, the simulated BrO VCD in Svalbard is generally $<6 \times 10^{13}$ molecular cm^{-2} and notably underestimates the measured BrO enhancements during March 17–18. Meanwhile, the simulated O_3 concentration in Mode1 is also flat at approximately 32 ppbv (Fig. 7). The correlation coefficient between Mode1 results and MAX-DOAS measurements is small, $R = 0.0018$ (Fig. S7a), demonstrating a poor connection between open-ocean sourced SSA and BrO. However, when the blowing-snow sourced SSA is taken into consideration, the simulation for this BEE and ODE are improved (Fig. 7), for example, simulated BrO VCD in Mode2 and Mode3 increase from 4.92×10^{13} molecular cm^{-2} and 6.97×10^{13} molecular cm^{-2} to 1.325×10^{14} molecular cm^{-2} and 1.478×10^{14} molecular cm^{-2} respectively between March 15 and 18 and the simulated surface ozone between March 17 and 18 drops below 20 ppbv. The correlation coefficients between the simulations and the measurements in March 2017 are $R = 0.69$ (for Mode2) and $R = 0.61$ (for Mode3) (Fig. S7b, c). Additionally, as indicated in Fig. 7, when open-ocean sourced SSA dominated the total SSA concentration, there was no BEE and ODE appeared in both simulations and measurements. After UTC 20:00 March 15, BrO VCD in Mode2, Mode3 and observations gradually grew to the peak value with the concentration of blowing-snow sourced SSA surged to 4.55 particle cm^{-3} accounting for 66.5% of the total SSA. During this period, surface ozone concentrations also decreased dramatically and an ODE occurred, which can further identify the role of blowing-snow sourced SSA in this specific case.

Svalbard was influenced by the low-pressure cyclone since March 14, however, the winds were not strong and could not result in BrO enhancements (as seen in both simulations and field observations). From March 15 to UTC 6:00 on March 16, surface wind speeds over sea ice covered areas north of Svalbard increased over 10 m s^{-1}, but MAX-DOAS detected no significant BrO enhancement (Fig. 2). The modeled SSA particle number densities show that in this period, the dominated SSA is mainly sea spray not blowing snow-sourced SSA (Fig. 7c). This is also confirmed by the airmasses back trajectory history data, showing that before UTC 6:00 on March 16, the airmasses originated from the Norwegian Sea. The lack of BrO in the open ocean originated air indicates that sea spray emitted from the open ocean does not significantly contribute to the build-up of BrO in the boundary layer. Since UTC 12:00 on March 16, the dominant wind directions changed to the northeast and the airmasses moved across sea ice covered areas under high surface wind speed (>10 m s^{-1}, Fig. 5c–d) which can be benefit for blowing-snow sourced SSA generation (Jones et al., 2009). Then the observed BrO VCD gradually increased and a significant ozone depletion also occurred with the transportation of the air masses across sea ice surface.

Fig. 8 shows the simulated BrO profile at 0–4 km under Mode1 and Mode2. It can be seen that the open-ocean-sourced SSA mainly contributes to aloft BrO at heights >1 km (Fig. 8a). The modeled BrO VMR in the boundary layer was very low. This is interesting, as the surface wind speed at the station during March 15 to UTC 6:00 on March 16 was relatively high (reaching ~15 m s^{-1}) and the surface wind speed over sea ice zones close to Svalbard was also above 10 m s^{-1}. This could possibly be attributed to the extended height of marine boundary layer over a warmer open water, as open water may contain more energy than sea ice. Therefore, sea spray generated over the open ocean can be lifted to a higher altitude, and bromine is then distributed over a large altitude range. In contrast, sea-ice-sourced BrO is mainly limited to a height of <1 km (Fig. 8b), and the simulated BrO VMR is >40 pptv from March 16 to 18.

However, the model-data discrepancies were large. For instance, the model simulates a large BrO enhancement on March 16, which is not clearly shown in the remote sensing datasets, implying the possible timing delay in the bromine release from the sea spray generated. In p-TOMCAT parameterization, the release of bromine from SSA occurs immediately (zero delay in time) following the production of SSA from open ocean and sea ice. This simplification may explain why the occurrence of simulated BEE is a few hours ahead of the reality, as shown in another BEE study (Zhao et al., 2016).

3.4. Sensitivity experiments

3.4.1. Influence of snow salinity

Most of this large BEE observed in March 2017 was successfully simulated by p-TOMCAT, but the model still overestimated the BrO. For example, the simulated tropospheric BrO (0–3 km) in Mode2 is approximately 1.4 times that of the MAX-DOAS BrO VCD. We attribute the overestimation is mainly due to the applying a 3.5 times Weddell Sea salinity to the Arctic (Yang et al., 2020; Yang et al., 2019). To investigate the model sensitivity, we performed a few experiments with different snow salinities for blowing snow. The salinity setups are presented in Table 2. When the snow salinity was reduced to 1-time (Mode2-1) and 2-time (Mode2-2) that of the Weddell Sea snow salinity, the regression slope of BrO VCD between the model and the observation reduced to ~0.6 and 0.9, respectively (Fig. S8b, c). Given that the control run salinity (3.5-time of the Weddell Sea snow salinity) is for the whole Arctic (Yang et al., 2019; Yang et al., 2008), which may not work for the Svalbard or its nearby areas due to the high precipitation (Førland et al., 1997), as they may dilute snow salts.

In addition to the likely overestimated salinity of blowing snow at Svalbard and the possible delayed timing of bromine release from blowing snow sourced SSA, other factors might also contribute to the model-data discrepancies. For example, they include (i) the coarse resolution of the

Table 2
Model setup in the simulation experiments performed.

Experiment ID	SSA and bromine schemes	Salinity of snow (×times the Weddell Sea snow salinity)	Sublimation rate (dm_i/dt)
Mode1	Only open-ocean sourced emission	x = 3.5	∝Constant (equivalent to the experiment named "SI_Base_A" in Yang et al., 2019)
Mode2	Only blowing-snow sourced emission		
Mode3	Both open-ocean and blowing-snow sourced emissions		
Mode2-1	Only blowing-snow sourced emission	x = 1	
Mode2-2		x = 2	
Mode2-3	Only blowing-snow sourced emission	x = 3.5	$\propto d_i$ (equivalent to the experiment named "SI_Classic_A" in Yang et al., 2019)

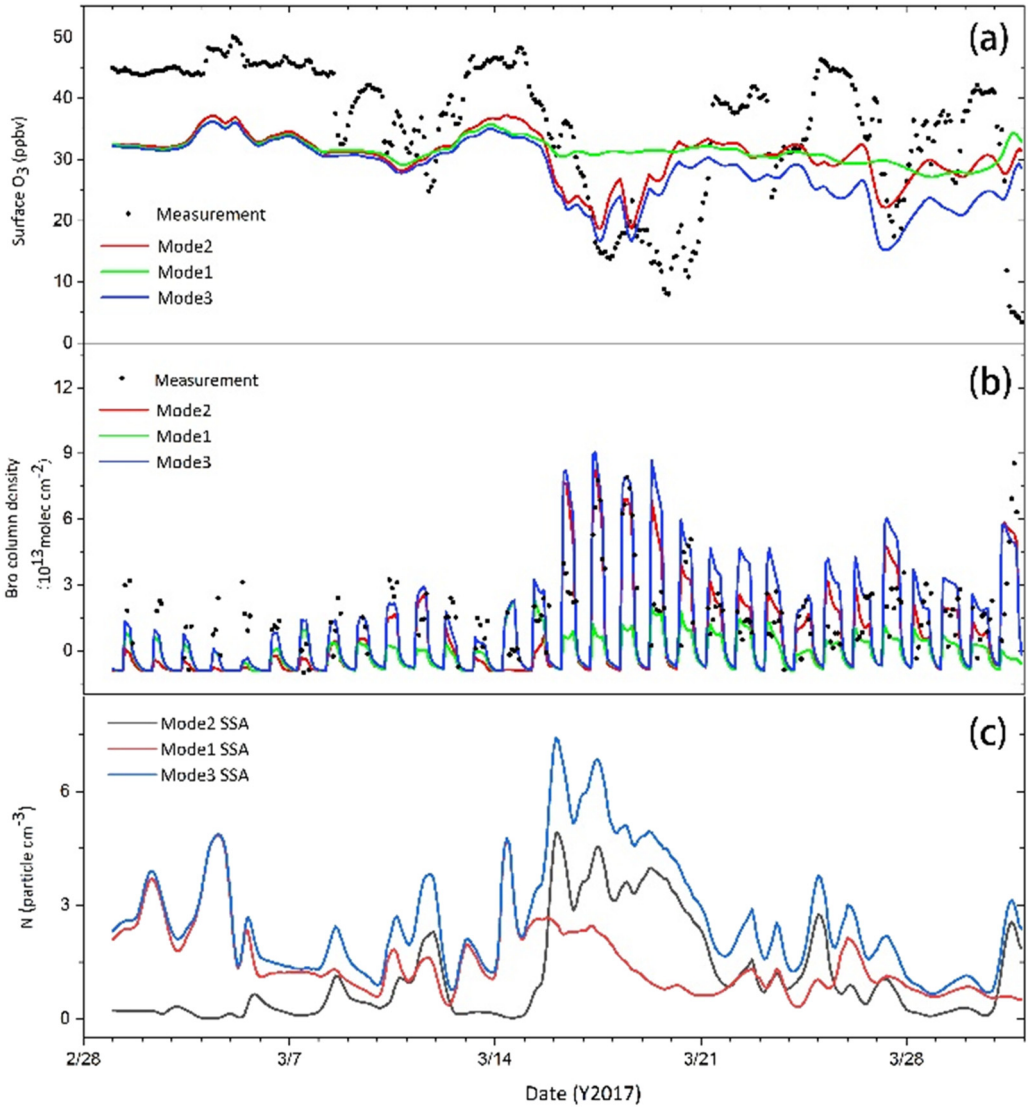

Fig. 7. (a)–(b) Time series of measured and modeled. (a) Surface ozone concentrations, (b) BrO vertical column densities. The spots indicate the measurements from March 1 to 31, the solid green line (Mode1) shows open-ocean sourced BrO column density, the solid red line (Mode2) shows blowing-snow sourced BrO column density, the solid blue line (Mode3) shows the sum of both sources results. (c) Simulated SSA particle number densities in the surface layer from three experiments. The black line (Mode1) represents the open-ocean sourced SSA; the red line (Mode2) represents the sea-ice sourced SSA, and the blue line (Mode3) is the sum of the two sources.

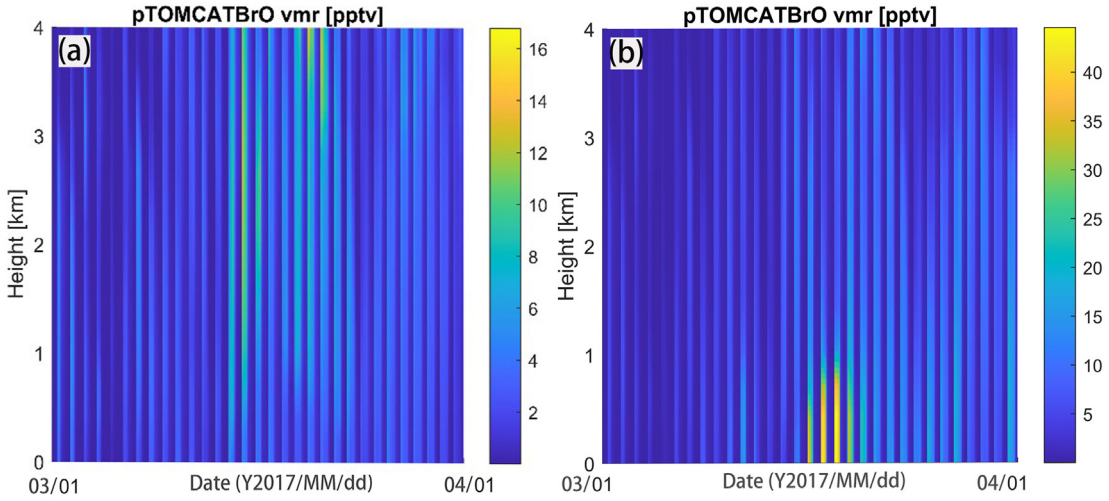

Fig. 8. Vertical profiles of modeled BrO concentration in (a) Mode1 and (b) Mode2.

model, which only represents average BrO over several hundred square km and the observed VCD of BrO only for at a point. (ii) The uncertainty of the transformation from MAX-DOAS BrO DSCD to VCD, which is sensitive to the optical path relative to the atmospheric visibility (Frieß et al., 2011). (iii) The possible difference in particle spectrum between the sea spray and blowing snow-sourced SSA, which is not yet known, but is critical in determining the lifetime and the reactive bromine release.

3.4.2. Influence of sublimation function

Considering the sublimation rate of particles is a significant factor linked to the release of SSA, another sensitivity experiment with two different calculations for SSA production fluxes was performed in this section. In Mode2 run, the snow particle loss rate (namely $\frac{dm_i}{dt}$) was controlled by the Kelvin curvature effect (Pruppacher and Klett, 2010), in which small particles lose mass at a rate faster than large ones. While, in Mode2-3 run, a loss rate function controlled by the moisture gradient between the snow particle and the ambient air was applied, resulting in fewer submicron-sized SSAs being produced (as mentioned in Yang et al., 2019). The accordingly outputs were shown in Fig. S9.

Referring to the correlation analysis, lower submicron-sized SSA production fluxes (Mode2-3) improved the correlation coefficient between modeled results and measurements compared with Mode2 (Fig. S9c), but the results of Mode2-3 also showed an underestimation for BrO with a slope of 0.511 (Fig. S9c). The lower submicron-sized SSA fluxes lead to a significant decrease by around 69% and the BrO partial column changed by maxima 59.9% (on March 17), which made the simulation results lower than measurements by 30%. Before March 16, the reduction of SSA by 69.9% can induce to a 52% decline of BrO partial column (Fig. S9a–b). These results indicate that the change of SSA production mechanism has a relatively large influence on BrO emission. However, due to the current field aerosol dataset from the Weddell Sea (Yang et al., 2019; Frey et al., 2020) only validate SSA production at size >0.4 μm, we are still lack of robust field data to pin-point the exact micro-physical processes involved in the SSA production from blowing snow, which forms the largest uncertainty regarding quantification of SSA production from sea ice in both size and number density.

4. Conclusions

Based on the observations of ground-based MAX-DOAS and satellite instruments, a significant BEE was observed during March 15–18, 2017, in Ny-Ålesund, Svalbard. During this bromine explosion event, the Svalbard archipelago and its eastern parts were constantly influenced by low-pressure systems that originated from the Norwegian Sea in the southwest of Svalbard. The HYSPLIT back trajectories show that the bromine-enriched air mass was transported across the northeastern area of Svalbard, which was mainly covered by first-year sea ice, before arriving in Ny-Ålesund.

Within the cyclones, the unstable boundary layer and high-level surface wind are conducive to generating blowing snow and accelerating the vertical mixing of lifted particles. The global chemical model p-TOMCAT can successfully reproduce the main feature of the BEE when blowing-snow-sourced SSA scheme was implemented. Additionally, we found that snow salinity is a key parameter in determining the magnitude of simulated BrO. Thus, precise measurement of the local surface snow salinity is necessary to enable a better model simulation.

Moreover, we found that this large bromine explosion event observed at Ny-Ålesund in mid-March 2017 was induced by a low-pressure cyclone, similar to the meteorological conditions referred to in some previous findings (e.g., Blechschmidt et al., 2016; Choi et al., 2018). When there is an unstable boundary layer condition over sea ice-covered regions, the SSA from blowing snow may play a significant role in the increment of BrO. Compared with blowing-snow sourced SSA, newly emitted SSA from open ocean seems not playing an immediate role in the BrO production because of its alkaline nature. However, because other possible mechanisms of bromine release are not included in the model, we could not quantify their contribution the increase of BrO from such as snowpack and open leads.

CRediT authorship contribution statement

Douxing Chen: Investigation, Methodology, Visualization, Formal analysis, Writing- Original draft preparation. **Yuhan Luo:** Conceptualization, Formal analysis, Funding acquisition, Writing - Review & Editing, Data curation. **Xin Yang:** Methodology, Formal analysis, Software, Visualization, Validation, Writing - Review & Editing. **Fuqi Si:** Resources, Project administration. **Ke Dou:** Resources, Data curation. **Haijin Zhou:** Resources, **Yuanyuan Qian:** Software. **Chunqiao Hu:** Software. **Jianguo Liu:** Funding acquisition, Supervision. **Wenqing Liu:** Supervision.

Declaration of competing interest

The authors declare that they have no known competing financial interests or personal relationships that could have appeared to influence the work reported in this paper.

Acknowledgments

This research was financially supported by the National Natural Science Foundation of China (Grant Nos. 41941011 and 41676184) and the Youth Innovation Promotion Association of CAS (Grant No. 2020439). XY thanks for the financial support by UK NERC funded project (NE/S00257X/1). The authors thank the organizations of the Chinese Arctic and Antarctic Administration (CAAA), Polar Research Institute of China, and teammates of the Chinese Arctic Yellow River Station for their kind help. We appreciate Andreas Richter and Ilias Bougoudis from the University of Bremen for providing the GOME-2B dataset. Sea ice information was provided by the NASA National Snow and Ice Data Center. The PANGAEA website provided meteorological data, and the ECMWF provided complementary data. Surface ozone data were obtained from the EBAS database. We gratefully acknowledge Caroline Fayt, Thomas Danckaert, and Michel van Roozendael from BIRA for providing the QDOAS analysis software. We also gratefully thank the NOAA Air Resources Laboratory (ARL) for the HYSPLIT transport model and READY website (http://www.ready.noaa.gov) used in this study.

Appendix A. Supplementary data

Supplementary data to this article can be found online at https://doi.org/10.1016/j.scitotenv.2022.156335.

References

Abbatt, J.P.D., Thomas, J.L., et al., 2012. Halogen activation via interactions with environmental ice and snow in the polar lower troposphere and other regions. Atmos. Chem. Phys. 12 (14), 6237–6271. https://doi.org/10.5194/acp-12-6237-2012.

Adams, J.W., Holmes, N.S., et al., 2002. Uptake and reaction of HOBr on frozen and dry NaCl/NaBr surfaces between 253 and 233 K. Atmos. Chem. Phys. 2, 79–91. https://doi.org/10.5194/acp-2-79-2002.

Barrie, L.A., Bottenheim, J.W., et al., 1988. Ozone destruction and photochemical-reactions at POLAR sunrise in the lower Arctic atmosphere. Nature 334 (6178), 138–141. https://doi.org/10.1038/334138a0.

Begoin, M., Richter, A., et al., 2010. Satellite observations of long range transport of a large BrO plume in the Arctic. Atmos. Chem. Phys. 10 (14), 6515–6526. https://doi.org/10.5194/acp-10-6515-2010.

Blechschmidt, A.M., Richter, A., et al., 2016. An exemplary case of a bromine explosion event linked to cyclone development in the Arctic. Atmos. Chem. Phys. 16 (3), 1773–1788. https://doi.org/10.5194/acp-16-1773-2016.

Bognar, K., Zhao, X., et al., 2020. Measurements of tropospheric bromine monoxide over four halogen activation seasons in the Canadian high Arctic. J. Geophys. Res. Atmos. 125, e2020JD033015. https://doi.org/10.1029/2020JD033015.

Bogumil, K., Orphal, J., et al., 2003. Measurements of molecular absorption spectra with the SCIAMACHY pre-flight model: instrument characterization and reference data for

atmospheric remote-sensing in the 230–2380 nm region. J. Photochem. Photobiol. A Chem. 157 (2–3), 167–184. https://doi.org/10.1016/S1010-6030(03)00062-5.
Bottenheim, J.W., Chan, E., 2006. A trajectory study into the origin of spring time Arctic boundary layer ozone depletion. J. Geophys. Res.-Atmos. 111 (D19), D19301. https://doi.org/10.1029/2006JD007055.
Bougoudis, I., Blechschmidt, A.-M., et al., 2020. Long-term time series of Arctic tropospheric BrO derived from UV–VIS satellite remote sensing and its relation to first-year sea ice. Atmos. Chem. Phys. 20 (20), 11869–11892. https://doi.org/10.5194/acp-20-11869-2020.
Brough, N., Jones, A.E., et al., 2019. Influence of sea ice-derived halogens on atmospheric HOx as observed in springtime coastal Antarctica. Geophys. Res. Lett. 46 (16), 10168–10176. https://doi.org/10.1029/2019GL083825.
Burrows, J.P., Platt, U., et al., 2011. Tropospheric remote sensing from space. In: Burrows, J.P., Platt, U., Borrell, P. (Eds.), The Remote Sensing of Tropospheric Composition From Space. Springer Verlag, Heidelberg, pp. 1–66.
Choi, S., Theys, N., et al., 2018. Link between Arctic tropospheric BrO explosion observed from space and sea-salt aerosols from blowing snow investigated using ozone monitoring instrument BrO data and GEOS-5 data assimilation system. J. Geophys. Res. Atmos. 123 (13), 6954–6983. https://doi.org/10.1029/2017jd026889.
Choi, S., Wang, Y., et al., 2012. Analysis of satellite-derived Arctic tropospheric BrO columns in conjunction with aircraft measurements during ARCTAS and ARCPAC. Atmos. Chem. Phys. 12 (3), 1255–1285. https://doi.org/10.5194/acp-12-1255-2012.
Errera, Q., Fonteyn, D., 2001. Four-dimensional variational chemical assimilation of CRISTA stratospheric measurements. J. Geophys. Res.-Atmos. 106 (D11), 12253–12265. https://doi.org/10.1029/2001JD900010.
Fleischmann, O.C., Hartmann, M., et al., 2004. New ultraviolet absorption cross-sections of BrO at atmospheric temperatures measured by time-windowing Fourier transform spectroscopy. J. Photochem. Photobiol. A Chem. 168 (1–2), 117–132. https://doi.org/10.1016/j.jphotochem.2004.03.026.
Førland, E.J., Hanssen-Bauer, I., et al., 1997. Climate statistics and long-term series of temperature and precipitation at Svalbard and Jan Mayen. MET Norway Rep. vol. 21/97, p. 72.
Frey, M.M., Norris, S.J., et al., 2020. First direct observation of sea salt aerosol production from blowing snow above sea ice. Atmos. Chem. Phys. 20 (4), 2549–2578. https://doi.org/10.5194/acp-20-2549-2020.
Frieß, U., Hollwedel, J., et al., 2004. Dynamics and chemistry of tropospheric bromine explosion events in the Antarctic coastal region. J. Geophys. Res.-Atmos. 109 (D6), D06305. https://doi.org/10.1029/2003JD004133.
Frieß, U., Sihler, H., et al., 2011. The vertical distribution of BrO and aerosols in the Arctic: measurements by active and passive differential optical absorption spectroscopy. J. Geophys. Res. 116, D00R04. https://doi.org/10.1029/2011jd015938.
Hendrick, F., Johnston, P.V., et al., 2008. One-decade trend analysis of stratospheric BrO over harestua (60 degrees N) and lauder (45 degrees S) reveals a decline. Geophys. Res. Lett. 35 (14), L14801. https://doi.org/10.1029/2008GL034154.
Holmes, C.D., Jacob, D.J., et al., 2010. Global atmospheric model for mercury including oxidation by bromine atoms. Atmos. Chem. Phys. 10 (24), 12037–12057. https://doi.org/10.5194/acp-10-12037-2010.
Hönninger, G., Leser, H., et al., 2004. Ground-based measurements of halogen oxides at the Hudson Bay by active longpath DOAS and passive MAX-DOAS. Geophys. Res. Lett. 31, L04111. https://doi.org/10.1029/2003gl018982.
Honninger, G., Platt, U., 2002. Observations of BrO and its vertical distribution during surface ozone depletion at alert. Atmos. Environ. 36 (15–16), 2481–2489. https://doi.org/10.1016/s1352-2310(02)00104-8.
Huang, J., Jaeglé, L., 2017. Wintertime enhancements of sea salt aerosol in polar regions consistent with a sea ice source from blowing snow. Atmos. Chem. Phys. 17 (5), 3699–3712. https://doi.org/10.5194/acp-17-3699-2017.
Huang, J., Jaeglé, L., et al., 2020. Evaluating the impact of blowing-snow sea salt aerosol on springtime BrO and O3 in the Arctic. Atmos. Chem. Phys. 20 (12), 7335–7358. https://doi.org/10.5194/acp-20-7335-2020.
Jones, A.E., Anderson, P.S., et al., 2009. BrO, blizzards, and drivers of polar tropospheric ozone depletion events. Atmos. Chem. Phys. 9 (14), 4639–4652. https://doi.org/10.5194/acp-9-4639-2009.
Kaleschke, L.A., Richter, J.B., et al., 2004. Frost flowers on sea ice as a source of sea salt and their influence on tropospheric halogen chemistry. Geophys. Res. Lett. 31 (16), L16114. https://doi.org/10.1029/2004gl020655.
Kalnay, E., Kanamitsu, M., et al., 1996. The NCEP/NCAR 40-year reanalysis project. Bull. Am. Meteorol. Soc. 77 (3), 437–471. https://doi.org/10.1175/1520-0477(1996)077<0437:TNYRP>2.0.CO;2.
Kromminga, H., Orphal, J., et al., 2003. New measurements of OClO absorption cross-sections in the 325–435 nm region and their temperature dependence between 213 and 293 K. J. Photochem. Photobiol. A Chem. 157 (2–3), 149–160. https://doi.org/10.1016/S1010-6030(03)00071-6.
Legrand, M., Yang, X., et al., 2016. Year-round records of sea salt, gaseous, and particulate inorganic bromine in the atmospheric boundary layer at coastal (Dumont d'Urville) and central (Concordia) East Antarctic sites. J. Geophys. Res.-Atmos. 121 (2), 997–1023. https://doi.org/10.1002/2015JD024066.
Levine, J.G., Yang, X., et al., 2014. Sea salt as an ice core proxy for past sea ice extent: a process-based model study. J. Geophys. Res. Atmos. 119 (9), 5737–5756. https://doi.org/10.1002/2013jd020925.
Luo, Y., Si, F., et al., 2018. Observations and source investigations of the boundary layer bromine monoxide (BrO) in the Ny-Ålesund Arctic. Atmos. Chem. Phys. 18 (13), 9789–9801. https://doi.org/10.5194/acp-18-9789-2018.
Marelle, L., Thomas, J.L., et al., 2021. Implementation and impacts of surface and blowing snow sources of Arctic bromine activation within WRF-Chem 4.1.1. J. Adv. Model Earth Syst. 13 (8), e2020MS002391. https://doi.org/10.1029/2020MS002391.
Maturilli, M., 2018. Continuous meteorological observations at station Ny-Ålesund (2017-03). Maturilli, M (2020): Continuous Meteorological Observations at Station Ny-Ålesund (2011-08 et seq). Alfred Wegener Institute - Research Unit Potsdam, PANGAEA https://doi.org/10.1594/PANGAEA.894597 Retrieved from.
Maturilli, M., 2018. Expanded Measurements FromStation Ny-Ålesund (2017-03). https://doi.org/10.1594/PANGAEA.887512 Retrieved from.
Morin, S., Savarino, J., et al., 2008. Tracing the origin and fate of NOx in the arctic atmosphere using stable isotopes in nitrate. Science 322 (5902), 730–732. https://doi.org/10.1126/science.1161910.
Oltmans, S.J., Schnell, R.C., et al., 1989. Seasonal surface ozone and filterable bromine relationship in the high Arctic. Atmos. Environ. 23 (11), 2431–2441. https://doi.org/10.1016/0004-6981(89)90254-0.
Peterson, P.K., Pöhler, D., et al., 2017. Observations of bromine monoxide transport in the Arctic sustained on aerosol particles. Atmos. Chem. Phys. 17 (12), 7567–7579. https://doi.org/10.5194/acp-17-7567-2017.
Peterson, P.K., Pöhler, D., et al., 2018. Springtime bromine activation over coastal and inland Arctic snowpacks. ACS Earth Space Chem. 2 (10), 1075–1086. https://doi.org/10.1021/acsearthspacechem.8b00083.
Peterson, P.K., Simpson, W.R., et al., 2015. Dependence of the vertical distribution of bromine monoxide in the lower troposphere on meteorological factors such as wind speed and stability. Atmos. Chem. Phys. 15 (4), 2119–2137. https://doi.org/10.5194/acp-15-2119-2015.
Platt, U., Stutz, J., 2008. Differential optical absorption spectroscopy. In: Stutz, U.P.a.J. (Ed.), Differential Optical Absorption Spectroscopy. Physics of Earth and Space Environments, pp. 135–174.
Pratt, K.A., Custard, K.D., et al., 2013. Photochemical production of molecular bromine in Arctic surface snowpacks. Nat. Geosci. 6 (5), 351–356. https://doi.org/10.1038/ngeo1779.
Pruppacher, H.R., Klett, J.D., 2010. Microphysics of Clouds and Precipitation. Springer, Dordrecht.
Rayner, N.A., Parker, D.E., et al., 2003. Global analyses of sea surface temperature, sea ice, and night marine air temperature since the late nineteenth century. J. Geophys. Res.-Atmos. 108 (D14), 4407. https://doi.org/10.1029/2002JD002670.
Rhodes, R.H., Yang, X., et al., 2018. Sea ice versus storms: what Controls Sea salt in Arctic ice Cores? Geophys. Res. Lett. 45 (11), 5572–5580. https://doi.org/10.1029/2018GL077403.
Rhodes, R.H., Yang, X., et al., 2017. Sea ice as a source of sea salt aerosol to Greenland ice cores: a model-based study. Atmos. Chem. Phys. 17 (15), 9417–9433. https://doi.org/10.5194/acp-17-9417-2017.
Sander, R., Keene, W.C., et al., 2003. Inorganic bromine in the marine boundary layer: a critical review. Atmos. Chem. Phys. 3, 1301–1336. https://doi.org/10.5194/acp-3-1301-2003.
Sihler, H., Platt, U., et al., 2012. Tropospheric BrO column densities in the Arctic derived from satellite: retrieval and comparison to ground-based measurements. Atmos.Meas.Tech. 5 (11), 2779–2807. https://doi.org/10.5194/amt-5-2779-2012.
Simpson, W.R., Brown, S.S., et al., 2015. Tropospheric halogen chemistry: sources, cycling, and impacts. Chem. Rev. 115 (10), 4035–4062. https://doi.org/10.1021/cr5006638.
Simpson, W.R., Carlson, D., et al., 2007a. First-Year Sea-ice contact predicts bromine monoxide (BrO) levels at Barrow, Alaska better than potential frost flower contact. Atmos. Chem. Phys. 7, 621–627. https://doi.org/10.5194/acp-7-621-2007.
Simpson, W.R., Glasow, R.V., et al., 2007. Halogens and their role in polar boundary-layer ozone depletion. Atmos. Chem. Phys. 7, 4375–4418. https://doi.org/10.5194/acp-7-4375-2007.
Simpson, W.R., Peterson, P.K., et al., 2017. Horizontal and vertical structure of reactive bromine events probed by bromine monoxide MAX-DOAS. Atmos. Chem. Phys. 17 (15), 9291–9309. https://doi.org/10.5194/acp-17-9291-2017.
Thalman, R., Volkamer, R., 2013. Temperature dependent absorption cross-sections of O-2-O-2 collision pairs between 340 and 630 nm and at atmospherically relevant pressure. Phys. Chem. Chem. Phys. 15 (37), 15371–15381. https://doi.org/10.1039/c3cp50968k.
Theys, N., Roozendael, M.V., et al., 2009. A global stratospheric bromine monoxide climatology based on the BASCOE chemical transport model. Atmos. Chem. Phys. 9, 831–848. https://doi.org/10.5194/acp-9-831-2009.
Theys, N., Van Roozendael, M., et al., 2011. Global observations of tropospheric BrO columns using GOME-2 satellite data. Atmos. Chem. Phys. 11 (4), 1791–1811. https://doi.org/10.5194/acp-11-1791-2011.
Toyota, K., McConnell, J.C., et al., 2011. Analysis of reactive bromine production and ozone depletion in the Arctic boundary layer using 3-D simulations with GEM-AQ: inference from synoptic-scale patterns. Atmos. Chem. Phys. 11 (8), 3949–3979. https://doi.org/10.5194/acp-11-3949-2011.
Toyota, K., McConnell, J.C., et al., 2014. Air–snowpack exchange of bromine, ozone and mercury in the springtime Arctic simulated by the 1-D model PHANTAS – part 1: in-snow bromine activation and its impact on ozone. Atmos. Chem. Phys. 14 (8), 4101–4133. https://doi.org/10.5194/acp-14-4101-2014.
Tschudi, M., Meier, W.N., et al., 2019. EASE-Grid Sea Ice Age, Version 4. [12 March to 18 March]. https://doi.org/10.5067/UTAV7490FEPB Retrieved from.
Van Dam, B., Helmig, D., et al., 2013. Springtime boundary layer O3and GEM depletion at Toolik Lake,Alaska. J. Geophys. Res. Atmos. 118 (8), 3382–3391. https://doi.org/10.1002/jgrd.50213.
Vandaele, A.C., Hermans, C., et al., 1998. Measurements of the NO2 absorption cross-section from 42 000 cm(-1) to 10 000 cm(-1) (238–1000 nm) at 220 K and 294 K. J. Quant. Spectrosc. Radiat. Transf. 59 (3–5), 171–184. https://doi.org/10.1016/S0022-4073(97)00168-4.
Vogt, R., Crutzen, P.J., et al., 1996. A mechanism for halogen release from sea-salt aerosol in the remote marine boundary layer. Nature 383 (6598), 327–330. https://doi.org/10.1038/383327a0.
Wagner, T., Burrows, J.P., et al., 2007. Comparison of box-air-mass-factors and radiances for multiple-Axis differential optical absorption spectroscopy (MAX-DOAS) geometries calculated from different UV/visible radiative transfer models. Atmos. Chem. Phys. 7 (7), 1809–1833. https://doi.org/10.5194/acp-7-1809-2007.

Wagner, T., Leue, C., et al., 2001. Spatial and temporal distribution of enhanced boundary layer BrO concentrations measured by the GOME instrument aboard ERS-2. J. Geophys. Res. Atmos. 106 (D20), 24225–24235. https://doi.org/10.1029/2000jd000201.

Warwick, N.J., Pyle, J.A., et al., 2006. Global modeling of biogenic bromocarbons. J. Geophys. Res.-Atmos. 111 (D24). https://doi.org/10.1029/2006JD007264.

Willis, M.D., Leaitch, W.R., et al., 2018. Processes controlling the composition and abundance of Arctic aerosol. Rev. Geophys. 56 (4), 621–671. https://doi.org/10.1029/2018rg000602.

Yang, X., Abraham, N.L., et al., 2014. How sensitive is the recovery of stratospheric ozone to changes in concentrations of very short-lived bromocarbons? Atmos. Chem. Phys. 14 (19), 10431–10438. https://doi.org/10.5194/acp-14-10431-2014.

Yang, X., Blechschmidt, A.-M., et al., 2020. Pan-Arctic surface ozone: modelling vs. measurements. Atmos. Chem. Phys. 20 (24), 15937–15967. https://doi.org/10.5194/acp-20-15937-2020.

Yang, X., Cox, R.A., et al., 2005. Tropospheric bromine chemistry and its impacts on ozone: a model study. J. Geophys. Res. 110 (D23), D23311. https://doi.org/10.1029/2005jd006244.

Yang, X., Frey, M.M., et al., 2019. Sea salt aerosol production via sublimating wind-blown saline snow particles over sea ice: parameterizations and relevant microphysical mechanisms. Atmos. Chem. Phys. 19 (13), 8407–8424. https://doi.org/10.5194/acp-19-8407-2019.

Yang, X., Pyle, J.A., et al., 2008. Sea salt aerosol production and bromine release: role of snow on sea ice. Geophys. Res. Lett. 35 (16), L16815. https://doi.org/10.1029/2008gl034536.

Yang, X., Pyle, J.A., et al., 2010. Snow-sourced bromine and its implications for polar tropospheric ozone. Atmos. Chem. Phys. 10 (16), 7763–7773. https://doi.org/10.5194/acp-10-7763-2010.

Zhao, X., Strong, K., et al., 2016. A case study of a transported bromine explosion event in the Canadian high arctic. Journal of Geophysical Research: Atmospheres 121 (1), 457–477. https://doi.org/10.1002/2015jd023711.

Zhenbo, C., Xuefa, S.H.I., et al., 2008. A survey of Norwegian Svalbard Islands and glacial geomorphology in the Arctic regions. Adv.Mar.Sci. 26 (2), 260–265.